Digest Journal of Nanomaterials and Biostructures

*Dig. J. Nanomater. Bios.* **2026**; 21(3): 53175
https://doi.org/10.31083/DJNB53175

*Original Research*

# Optical and Magnetic Properties of Mg-Doped Cobalt Ferrite ($Co_{1-x}Mg_xFe_2O_4$) Nanoparticles

Nasma A. Jaber[1], Ali K. Attia[1], Aliaa M. Zaki[1], Ghaiath A. Fadhil[2,*]

[1]Medical Physics Department, College of Science, Al-Karkh University of Science, 10001 Baghdad, Iraq
[2]Civil Engineering Department, College of Engineering, Al-Karkh University of Science, 10001 Baghdad, Iraq
*Correspondence: ghaiath.fadhil@kus.edu.iq (Ghaiath A. Fadhil)

Academic Editor: Karol Kyzioł
Submitted: 22 April 2026 Revised: 29 May 2026 Accepted: 24 June 2026 Published: 15 September 2026

**Abstract**

**Background:** Mg-doped cobalt ferrite ($Co_{1-x}Mg_xFe_2O_4$, $x$ = 0, 0.2, 0.4, 0.6, and 0.8) nanoparticles were investigated to evaluate the influence of $Mg^{2+}$ substitution on the structural, optical, and magnetic properties of cobalt ferrites. **Methods:** $Co_{1-x}Mg_xFe_2O_4$ nanoparticles were synthesized using the sol–gel autocombustion method and characterized by scanning electron microscopy, X-ray diffraction, Fourier transform infrared spectroscopy, ultraviolet–visible spectroscopy, and vibrating sample magnetometry. **Results:** Mg doping preserved the cubic spinel structure but caused redistribution of $Fe^{3+}$ ions between tetrahedral and octahedral sites, resulting in a slight change in the lattice constant. The X-ray density decreased from 5.68 to 4.83 g/cm$^3$ as $x$ increased from 0 to 0.8, while the optical bandgap increased from 1.75 to 2.3 eV. Fourier transform infrared spectra exhibited two characteristic absorption bands (400–600 cm$^{-1}$) corresponding to tetrahedral- and octahedral-site metal–oxygen bonds. $Mg^{2+}$ substitution altered the distribution of $Mg^{2+}$ and $Fe^{3+}$ ions among crystallographic sites and consequently modified the magnetic properties. **Conclusions:** $Mg^{2+}$ doping effectively modified the structural, optical, and magnetic properties of $CoFe_2O_4$ nanoparticles while preserving the spinel structure. These findings demonstrate that Mg substitution provides an effective approach for tailoring the functional properties of cobalt ferrites for optoelectronic and magnetic applications.

**Keywords:** $Mg^{2+}$ doping; cobalt ferrite; spinel ferrite; sol–gel autocombustion; nanoparticles; magnetic properties; optical properties; bandgap

## 1. Introduction

$CoFe_2O_4$ is a spinel ferrite with advantageous optical, electrical, and magnetic properties, which include high coercivity, moderate saturation magnetization, high magnetocrystalline anisotropy and Curie temperature, and structural and chemical stability [1,2] and are influenced by grain size and cation distribution between tetrahedral and octahedral sites [3]. $Co^{2+}$ ions preferentially occupy octahedral sites, whereas $Fe^{3+}$ ions are distributed across both tetrahedral and octahedral sites. This cation arrangement leads to strong antiferromagnetic coupling between Co and Fe sublattices, thus causing high magnetic coercivity and moderate magnetization [1,2,3]. Such properties make $CoFe_2O_4$ suitable for magnetic recording, microwave devices, magnetooptics, and sensing.

Many studies have systematically investigated the possibility of tailoring $CoFe_2O_4$ properties to increase energy efficiency and reduce costs in specific applications [2,3,4,5,6]. The doping of metal ions into $CoFe_2O_4$ can enable precise control over structural, electronic, and magnetic properties while maintaining the spinel structure [2,3,4,5,6]. For example, $Zn^{2+}$ doping increases the saturation magnetization ($M_s$) of $CoFe_2O_4$ and lowers its coercivity ($H_c$) [3]. However, excessive $Zn^{2+}$ doping diminishes structural stability and magnetic coupling between ferromagnetic ions. $Ni^{2+}$ doping, similarly, reduces the $H_c$ of $CoFe_2O_4$ because of the preference of $Ni^{2+}$ for octahedral sites [4], which limits the hard-magnetic applications of Ni-doped $CoFe_2O_4$. $Mn^{2+}$ and $Cu^{2+}$ exert similar effects on $H_c$ at low doping levels and cause structural instability at high levels [5]. $Mg^{2+}$ ions are nonmagnetic and have a radius comparable with that of $Co^{2+}$ [6], thus having the capacity to modify the remanent magnetization ($M_r$) and $H_c$ of $CoFe_2O_4$ without inducing marked structural disturbances. Furthermore, $Mg^{2+}$ ions prefer to occupy octahedral sites, which are occupied by $Fe^{3+}$ and $Co^{2+}$ in $CoFe_2O_4$ [1,2,3,4,5]. The redistribution of $Fe^{3+}$, $Co^{2+}$ and $Mg^{2+}$ ions in $CoFe_2O_4$ upon $Mg^{2+}$ doping and its impact on optical and magnetic properties remain underexplored.

The selection of an appropriate processing method is vital for the effective and sustainable $Mg^{2+}$ doping of $CoFe_2O_4$ nanoparticles. The sol–gel method is widely used for $CoFe_2O_4$ doping because it produces structures with chemical uniformity [6]. Hydrothermal methods afford Mg-doped ferrite nanoparticles with tunable surface morphology and high crystallinity [7], while microwave-assisted routes offer the benefits of shorter reaction times and lower costs [8]. Thermal decomposition can be used to produce uniformly sized nanoparticles [9], and flame-based techniques have been explored for large-scale pro-

duction [10]. Given that each of these methods has certain drawbacks, recent research has focused on hybrid synthesis routes enabling the efficient control of structural and functional properties [11]. The sol–gel autocombustion method is a wet chemical route combining the benefits of sol–gel and combustion processes [12,13], e.g., the uniform distribution of doping elements, nanoscale particles, and low energy consumption [14], and has been used to prepare $CoFe_2O_4$ nanoparticles doped with Al, Ni, Nd, and Zn [15]. Previous studies on Mg-doped $CoFe_2O_4$ nanoparticles produced via sol–gel autocombustion method, the coupled influence of $Mg^{2+}$ substitution on the structural, optical, and magnetic properties over a broad composition range remains insufficiently understood. In particular, the relationship between cation redistribution and the resulting functional properties. Hence, we selected this method to prepare Mg-doped $CoFe_2O_4$ ($Co_{1-x}Mg_xFe_2O_4$, $x$ = 0, 0.2, 0.4, 0.6, and 0.8) nanoparticles and examined the impact of doping extent ($x$) on structural, optical, and magnetic properties to understand the influence of Mg doping on lattice parameters, ion distribution, and magnetic interactions. By evaluating doping-induced changes, we established a correlation between $Mg^{2+}$ substitution, structural modification, optical bandgap variation, and magnetic behavior within a single experimental framework. The obtained insights improve our understanding of doping mechanisms and enable the compositional fine-tuning of doped $CoFe_2O_4$ nanoparticles for functional magnetic applications.

## 2. Materials and Methods

$Co(NO_3)_2 \cdot 6H_2O$, $Mg(NO_3)_2 \cdot 6H_2O$, and $Fe(NO_3)_3 \cdot 6H_2O$ (all 99.99% pure), Citric acid monohydrate, Aqueous ammonia (99 wt%), and distilled water were sourced from a local provider (Uma Company). $Co(NO_3)_2 \cdot 6H_2O$ ($1 - x$ mol), $Mg(NO_3)_2 \cdot 6H_2O$ ($x$ mol), $Fe(NO_3)_3 \cdot 6H_2O$ (2 mol), and citric acid monohydrate (3 mol) were dissolved in distilled water (100 mL) upon stirring (magnetic hot plate stirrer, HoverLabs, model SH-2, Ambala Cantt, India) for 1 h at room temperature. The resulting transparent solution was dropwise supplemented with aqueous ammonia to reach pH 7 and heated at 80 °C under constant stirring for 2 h. The thus produced homogeneous gel was oven-dried at 180 °C for 15 min, and the residue was crushed using a mortar, annealed in air in a furnace at 800 °C for 1 h, and cooled to room temperature to obtain $Co_{1-x}Mg_xFe_2O_4$ as a crystalline powder.

Surface morphology was probed using field emission scanning electron microscopy (SEM; Inspect F50, Thermo Fisher Scientific, Inc., Hillsboro, OR, USA), crystal structure and phase purity were probed using X-ray diffraction (XRD; Rigaku Ultima IV, Tokyo, Japan, Cu $K_\alpha$ radiation with $\lambda$ = 1.5406 Å, Start Position: 19.34°, End Position: 79.99°, Step Size: 0.05°, Scan Step Time: 1.0 s), and crystallite size was calculated using the Scherrer equation [10]. The formation of metal–oxygen bonds was confirmed using Fourier transform infrared (FTIR) spectroscopy (Shimadzu Corporation, Kyoto, Japan), with spectra recorded in the range of 400–4000 $cm^{-1}$. Ultraviolet–visible absorption spectra (CARY 100 Conc. spectrometer, Agilent Technologies, Inc., Santa Clara, CA, USA) were recorded for aqueous dispersions within a wavelength range of 200–1100 nm. Magnetic properties were characterized using vibrating sample magnetometry (model EV-7, MicroSense, Lowell, MA, USA). Unless stated otherwise, characterizations were performed at room temperature.

## 3. Results

### *3.1 Structural Properties*

Particle agglomeration was observed in all samples (Fig. 1) and ascribed to strong magnetic interactions among particles. Furthermore, the conductive Au layer applied prior to SEM imaging partially covered fine morphological details, which complicated the identification of particle boundaries. Hence, SEM imaging was used to analyze general morphology rather than perform precise particle size comparison.

The XRD patterns of all samples (Fig. 2) matched that of $CoFe_2O_4$ (PDF Card No. 00-002-1045) for Cu $K_\alpha$ radiation ($\lambda$ = 1.5406 Å) [6,16]. The weak secondary peaks at $2\theta$ = 50°, 70°, and 75° were ascribed to secondary phases such as $Fe_2O_3$, CoO, and MgO. Thus, the spinel structure (Fd-3m space group) was maintained in all samples [6], which confirmed that the incorporation of $Mg^{2+}$ caused no lattice disruption and suggested that the substitution of $Co^{2+}$ by $Mg^{2+}$ occurred through doping rather than a phase transition. The small shift in peak positions with increasing $x$ was attributed to the minor difference between the ionic radii of $Mg^{2+}$ and $Co^{2+}$ and may be related to the abovementioned preference of $Mg^{2+}$ for octahedral sites. This preference led to the swapping of $Fe^{3+}$ ions between local octahedral and tetrahedral sites and could have affected metal–oxygen bond lengths. FTIR spectroscopic analysis confirmed these structural changes, as outlined later.

Interplanar spacings and lattice parameters were estimated using the tetrahedral lattice interplanar spacing equation [17,18]. The lattice parameters varied with $x$, which confirmed that doping caused lattice distortion (Table 1). Notably, the effect of $x$ on experimental lattice parameters was smaller than that on theoretical lattice parameters, which reflects the adaptation of the spinel structure to compositional changes and suggests that structural distortion occurred uniformly throughout the crystal rather than being localized.

Crystal density decreased with increasing $x$ because of the higher atomic weight of Co compared with that of Mg [6]. The crystallite size of $Co_{1-x}Mg_xFe_2O_4$—calculated from the full width at half maximum of the (311) peak using Scherrer's equation [19]—decreased with increasing $x$ (Table 1). This reduction was attributed to the difference in ionic radii between $Mg^{2+}$ and $Co^{2+}$, which inhibited crystal

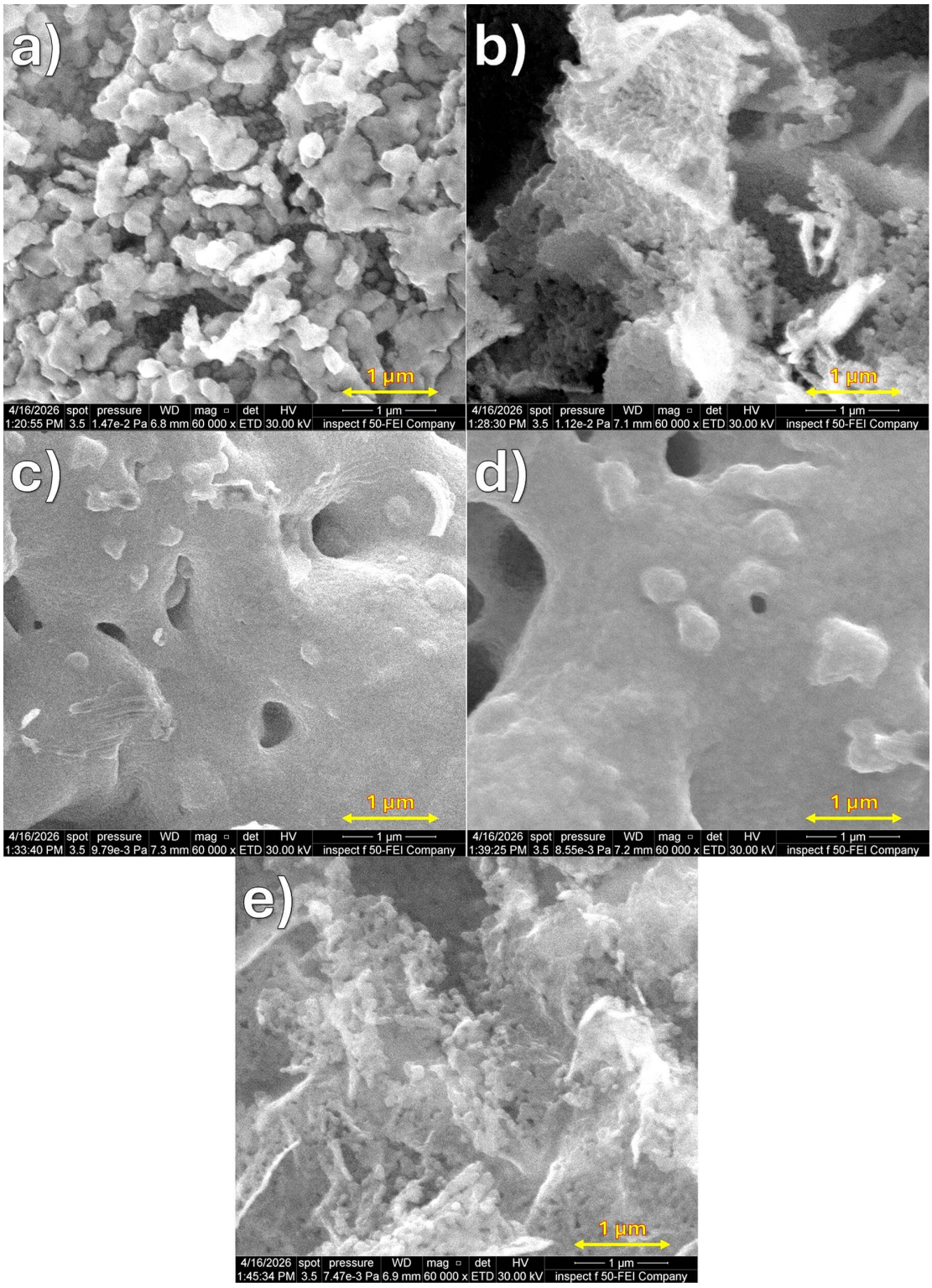


**Fig. 1. SEM images of $Co_{1-x}Mg_xFe_2O_4$ samples with $x$ = (a) 0, (b) 0.2, (c) 0.4, (d) 0.6, and (e) 0.8**. The corresponding scale bars are 1 µm. SEM, scanning electron microscopy.

growth and increased the density of defects in the crystal lattice. The distribution of ions in the spinel structure also contributed to the decrease in crystallite size, as $Mg^{2+}$ occupied positions different from those occupied by $Co^{2+}$. The increase in crystallite size at $x$ = 0.6 was attributed to enhanced crystallinity and reduced crystal defect content. The findings were compared with those of previous studies for validation (Table 2, Ref [2,6,16,18]).

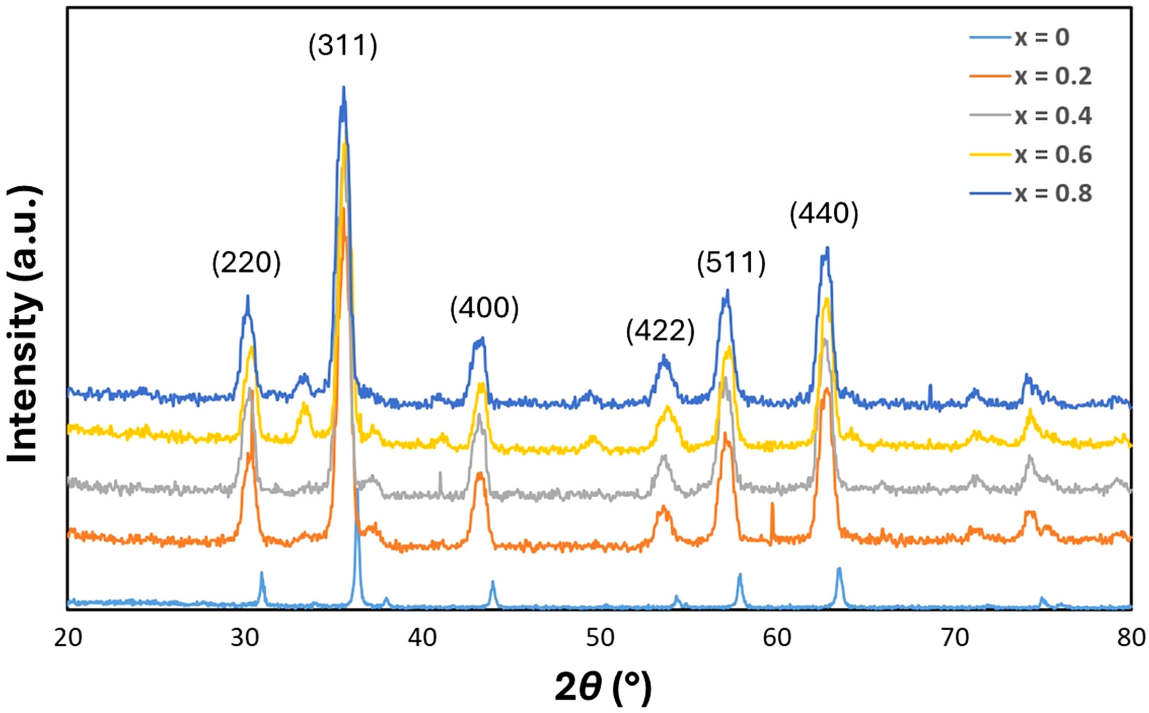


**Fig. 2. XRD patterns of $Co_{1-x}Mg_xFe_2O_4$.** $2\theta$, diffraction angle; XRD, X-ray diffraction.

**Table 1. Structural properties of $Co_{1-x}Mg_xFe_2O_4$ extracted from XRD patterns.**

| $x$ | $d$ (Å) | $2\theta$ (°) | $B$ (°) | $a_{exp}$ (Å) | $a_{th}$ (Å) | $d_x$ (g/cm$^3$) | $D$ (nm) | $L_A$ (Å) | $L_B$ (Å) |
|---|---|---|---|---|---|---|---|---|---|
| 0 | 2.470 | 36.36 | 0.21 | 8.20 | 6.98 | 5.68 | 74.10 | 3.50 | 2.98 |
| 0.2 | 2.520 | 35.68 | 0.37 | 8.36 | 7.12 | 5.22 | 45.60 | 3.62 | 2.96 |
| 0.4 | 2.511 | 35.74 | 0.78 | 8.33 | 7.23 | 5.10 | 19.89 | 3.61 | 2.95 |
| 0.6 | 2.506 | 35.83 | 0.39 | 8.32 | 7.57 | 4.90 | 39.95 | 3.60 | 2.94 |
| 0.8 | 2.500 | 35.75 | 0.79 | 8.30 | 7.61 | 4.83 | 19.71 | 3.59 | 2.93 |

$d$, interplanar spacing; $B$, full width at half maximum; $a_{exp}$, experimentally calculated lattice parameter; $a_{th}$, theoretically calculated lattice parameter; $d_x$, density; $D$, crystallite size; $L_A$, hopping length at tetrahedral sites; $L_B$, hopping length at octahedral sites.

**Table 2. Structural parameters of $Co_{1-x}Mg_xFe_2O_4$ reported in previous studies.**

| $x$ | $a_{exp}$ (Å) | $d_x$ (g/cm$^3$) | $D$ (nm) | Reference |
|---|---|---|---|---|
| 0 | 8.370 | 5.305 | 9.20 | [2] |
| 0 | 8.360 | - | 54.00 | [6] |
| 0 | 8.186 | 5.630 | 29.33 | [16] |
| 0.5 | - | - | 29 | [18] |

### *3.2 Optical Properties*

The absorption spectra of all samples extended from the ultraviolet region to the visible and near-infrared regions (Fig. 3) and were therefore characteristic of spinel ferrite nanomaterials [20]. The increased absorbance at lower wavelengths observed for all samples indicated the presence of electronic transition mechanisms. The higher absorbance observed for the non-doped sample was ascribed to its stronger $Fe^{3+}$–O and $Co^{2+}$–O transitions. The change in absorbance with increasing $x$—a direct consequence of replacing $Co^{2+}$ with $Mg^{2+}$—was more noticeable in the visible region.

The change in optical properties with increasing $x$ confirmed the doping-induced modification of the electronic structure of the spinel lattice. The introduction of $Mg^{2+}$ distorted the crystal field around $Fe^{3+}$ and thus widened the optical bandgap. The higher absorbance at longer wavelengths suggests that $Mg^{2+}$ doping reduced the optical absorption capacity. This behavior is beneficial for applications that combine optical and magnetic behavior [19]. Optical bandgaps were determined using the Tauc plot method (Fig. 4), namely from the $x$-intercepts of the extrapolated linear fits of $(\alpha h\nu)^2$ vs. $h\nu$ plots, where α is the absorption coefficient, $h$ is Planck's constant, $\nu$ is the photon frequency, and $h\nu$ is the photon energy. This method is widely used for semiconductor materials [3]. The bandgap increased from 1.75 eV at $x$ = 0 to 2.30 eV at $x$ = 0.8 (Table

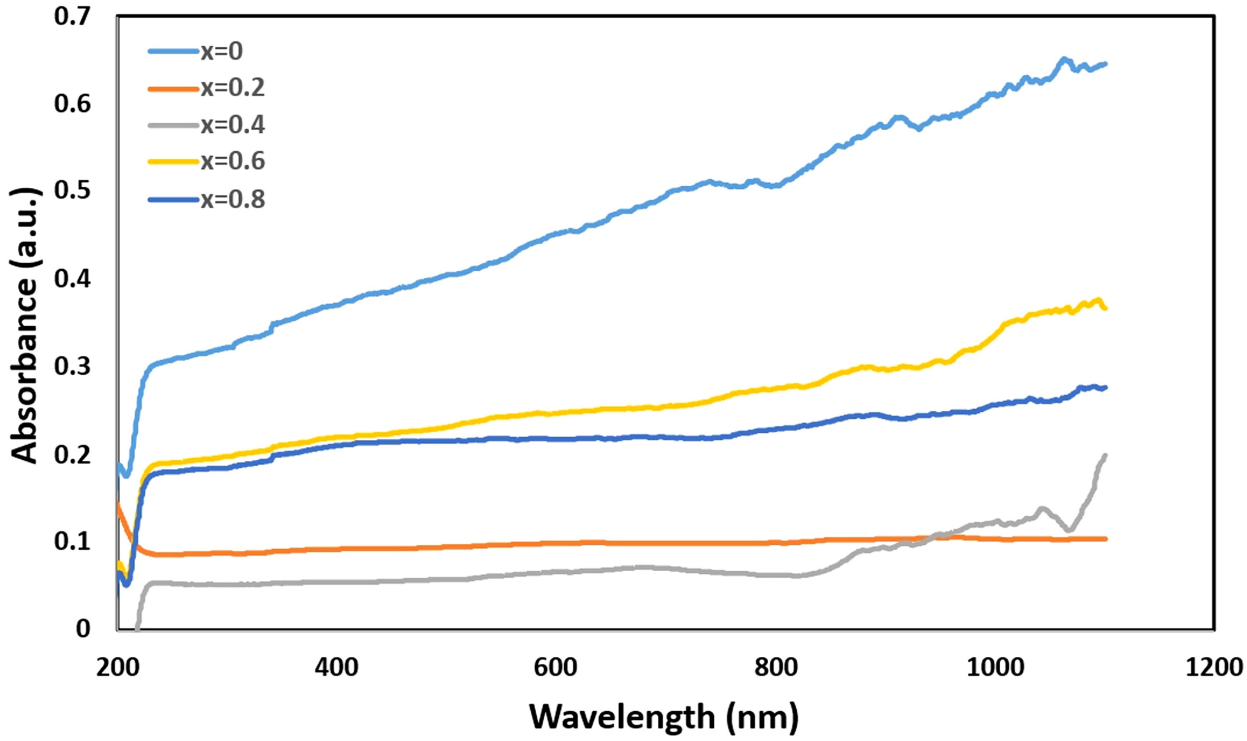


**Fig. 3. Ultraviolet–visible spectra of $Co_{1-x}Mg_xFe_2O_4$.**

3), attributed to the doping-induced modification of the energy levels of Co 3d orbitals near the conduction band edge, reduced crystallite size and crystal defect density, and quantum confinement effects [16]. These results align with previous findings indicating that the doping of ferrites with divalent ions such as $Mg^{2+}$ increases the bandgap [17]. Such behavior is related to defect state reduction and lattice regularity enhancement. Doping enhanced insulating behavior, thus holding promise for applications requiring low conductivity [18].

**Table 3. Optical bandgaps of $Co_{1-x}Mg_xFe_2O_4$.**

| $x$ | Optical bandgap (eV) |
|---|---|
| 0 | 1.75 |
| 0.2 | 1.90 |
| 0.4 | 2.00 |
| 0.6 | 2.15 |
| 0.8 | 2.30 |

The discrepancy between the bandgap at $x$ = 0 obtained herein (1.75 eV) and that reported previously (1.17 eV) [3] was ascribed to differences in preparation conditions, e.g., annealing temperature. Additionally, the bandgap increased upon $Mg^{2+}$ doping, which aligns with the results obtained herein. Fig. 5 illustrates the relationship between reflectivity $R$ and wavelength [8]. The increase in $R$ with increasing $x$ was ascribed to the concomitant changes in the electron distribution between the tetrahedral (A) and octahedral (B) sites and the resulting decrease in the probability of d–d electronic transitions. Similarly, bandgap widening increased reflectivity. The decrease in absorbance and increase in reflectivity with increasing $x$ directly affected the transmittance of cobalt ferrite, which is opaque. Specifically, transmittance was positively correlated with $x$. Higher transmittance was accompanied by a wider bandgap and hence, lower conductivity and higher resistivity.

FTIR spectra confirmed the spinel structure of all samples (Fig. 6), as evidenced by the presence of characteristic stretching vibrations for bonds between oxygen and metals at tetrahedral (550–600 $cm^{-1}$) and octahedral (400–500 $cm^{-1}$) sites [6]. Thus, $Mg^{2+}$ doping did not markedly affect the lattice structure. The broad band around 3400 $cm^{-1}$ was attributed to the O–H stretching vibrations of hydroxyl groups and adsorbed water molecules, while the weaker band near 1600 $cm^{-1}$ was ascribed to H–O–H bending vibrations. The absorption bands around 1384 and 1037 $cm^{-1}$ may be related to residual nitrate and/or organic groups originating from the synthesis process.

The slight shift in the octahedral vibration region at high $x$ (Table 4) confirmed that $Mg^{2+}$ ions preferentially occupied octahedral sites in the spinel lattice. The shift of the tetrahedral vibration band suggests redistribution of $Fe^{3+}$ ions between the tetrahedral (A) and octahedral (B) sites to maintain charge balance within the spinel lattice. These findings agree with the structural analysis results presented earlier.

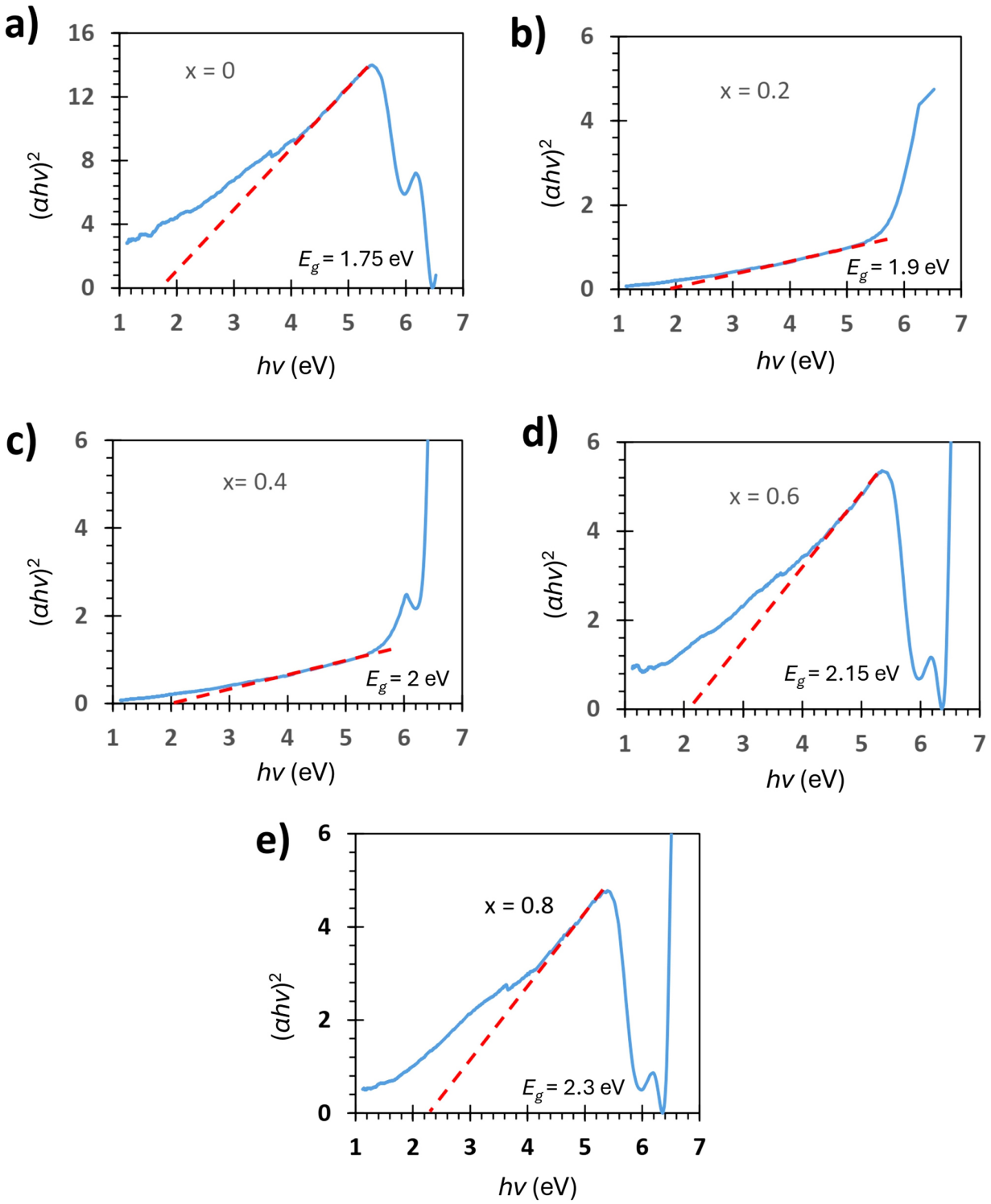


**Fig. 4. Tauc plots used to determine the optical bandgap ($E_g$) of $Co_{1-x}Mg_xFe_2O_4$ samples with $x$ = (a) 0, (b) 0.2, (c) 0.4, (d) 0.6, and (e) 0.8.**

**Table 4. Positions of the selected FTIR peaks of $Co_{1-x}Mg_xFe_2O_4$.**

| Mode | $x = 0$ | $x = 0.2$ | $x = 0.4$ | $x = 0.6$ | $x = 0.8$ |
|---|---|---|---|---|---|
| Tetrahedral-site M–O ($cm^{-1}$) | 576.72 | 567.07 | 570.93 | 559.36 | 561.29 |
| Octahedral-site M–O ($cm^{-1}$) | 462.91 | 472.56 | 412.77 | 466.77 | 422.41 |

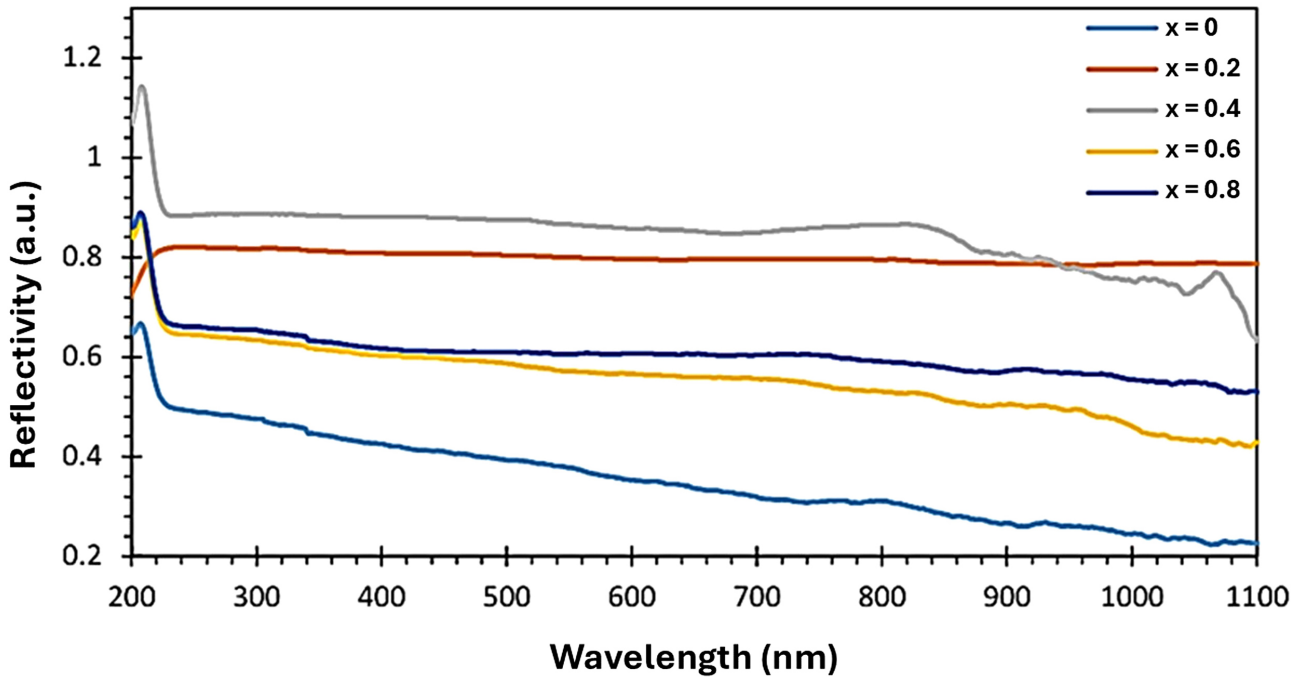


**Fig. 5. Reflectivity–wavelength plots of $Co_{1-x}Mg_xFe_2O_4$ samples with $x$ = 0, 0.2, 0.4, 0.6, and 0.8.**

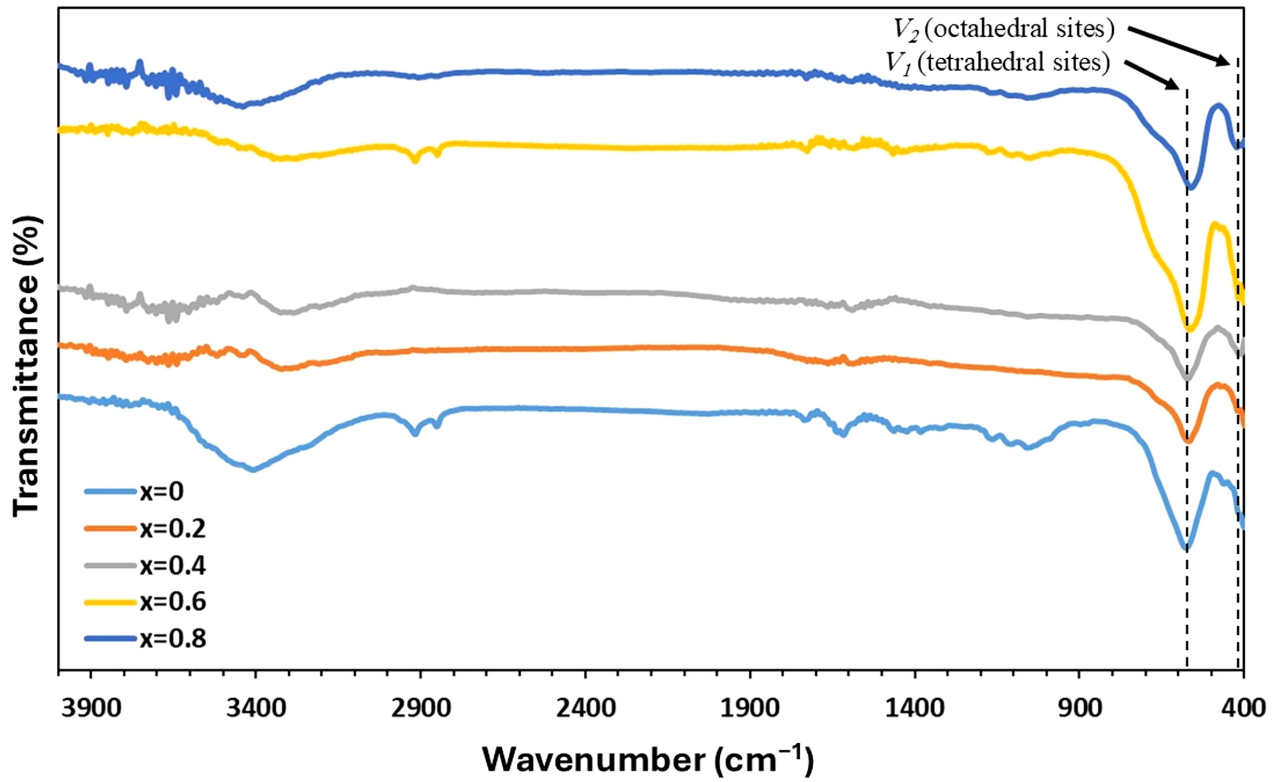


**Fig. 6. FTIR spectra of $Co_{1-x}Mg_xFe_2O_4$.** FTIR, Fourier transform infrared.

The positions of the FTIR bands were used to calculate force constants and Debye temperatures (Table 5). The force constants (and hence, interatomic bonding strength), bond angles, and interionic distances varied with $x$. The Debye temperature ($\Theta_D$) values varied with different $Mg^{2+}$ content, with an overall reduction from 747.9 K at $x$ = 0 to 707.67 K at $x$ = 0.8, which was linked to the concomitant shift of tetrahedral-site Mg–O peaks to lower wavenumbers

**Table 5. Selected parameters determined from the FTIR spectra of $Co_{1-x}Mg_xFe_2O_4$.**

| $x$ | $V_1$ ($cm^{-1}$) | $V_2$ ($cm^{-1}$) | $V_{ave}$ ($cm^{-1}$) | $F_1 \times 10^2$ (N/m) | $F_2 \times 10^2$ (N/m) | $F_{ave} \times 10^2$ (N/m) | $\Theta_D$ (K) |
|---|---|---|---|---|---|---|---|
| 0 | 576.72 | 462.92 | 519.82 | 2.4 | 1.5 | 1.95 | 747.9 |
| 0.2 | 576.07 | 472.56 | 524.32 | 2.34 | 1.6 | 1.97 | 754.17 |
| 0.4 | 570.93 | 412.77 | 491.85 | 2.37 | 1.24 | 1.8 | 707.67 |
| 0.6 | 559.36 | 466.77 | 513.1 | 2.27 | 1.58 | 1.92 | 738.2 |
| 0.8 | 561.29 | 422.41 | 491.85 | 2.29 | 1.29 | 1.79 | 707.67 |

$V_1$, higher-frequency absorption band; $V_2$, lower-frequency absorption band; $V_{ave}$, average absorption frequency; $F_1$, $F_2$, and $F_{ave}$, tetrahedral-site, octahedral-site, and average force constants, respectively; $\Theta_D$, Debye temperature.

**Table 6. Selected parameters determined from the FTIR spectra of $Co_{1-x}Mg_xFe_2O_4$ in previous studies.**

| $x$ | $V_1$ ($cm^{-1}$) | $V_2$ ($cm^{-1}$) | $F_1 \times 10^2$ (N/m) | $F_2 \times 10^2$ (N/m) | $\Theta_D$ (K) | Reference |
|---|---|---|---|---|---|---|
| 0 | 548.0 | 343.00 | 2.200 | 0.860 | - | [2] |
| 0 | 542.0 | 360.00 | - | - | 649.2 | [3] |
| 0 | 595.2 | 419.26 | - | - | - | [5] |
| 0.5 | 588. 3 | 432.10 | 1.266 | 1.076 | - | [6] |

**Table 7. Selected magnetic properties of $Co_{1-x}Mg_xFe_2O_4$ determined herein.**

| $x$ | $M_s$ (emu/g) | $M_r$ (emu/g) | $H_c$ (Oe) | $M_r/M_s$ | $K_1 \times 10^3$ ($J/m^3$) | $\mu_i$ | $\mu_B$ |
|---|---|---|---|---|---|---|---|
| 0 | 22.65 | 11.5 | 1650 | 0.5 | 4.89 | 334.53 | 0.92 |
| 0.2 | 16.8 | 9.31 | 1070 | 0.55 | 2.35 | 431.43 | 0.71 |
| 0.4 | 12.83 | 8.6 | 610 | 0.67 | 1.03 | 101.99 | 0.51 |
| 0.6 | 9.94 | 6.1 | 510 | 0.61 | 0.663 | 23.92 | 0.37 |
| 0.8 | 8.3 | 2.4 | 145 | 0.29 | 0.158 | 69.24 | 0.32 |

$M_s$, saturation magnetization; $M_r$, remanent magnetization; $H_c$, coercivity; $K_1$, magnetocrystalline anisotropy constant; $M_r/M_s$, squareness ratio; $\mu_B$, magnetic moment per formula unit; $\mu_i$, initial permeability.

[3,20]. Table 6 (Ref. [2,3,5,6]) compares the obtained results with those of previous studies.

### *3.3 Magnetic Properties*

Hysteresis loops showed a strong response to $Mg^{2+}$ doping (Fig. 7). $M_s$ decreased with increasing $x$ (Table 7) because of the concomitant decrease in magnetic moment due to lower Co content. The decrease in $H_c$ with increasing $x$ was attributed to the concomitant weakening of magnetocrystalline anisotropy. This behavior was consistent with that in previous studies [18,21]. At $x$ = 0.8, near-superparamagnetic behavior due to low magnetocrystalline anisotropy was observed. The hysteresis loops exhibited a slight inflection, which was attributed to the characteristic magnetic behavior of Mg-doped $CoFe_2O_4$ nanoparticles [21]. $Mg^{2+}$ ions reduced the contribution of the octahedral sites to the overall magnetic moment, thereby altering magnetic properties [18]. This is a consequence of reduced spin–orbit coupling in these crystals resulting from the substitution of ferromagnetic $Co^{2+}$ with nonmagnetic $Mg^{2+}$.

The formation of single-domain randomly oriented nanostructures with uniaxial anisotropy is beneficial for many applications, such as gas sensors and magnetic fluids [16], and was quantified in terms of the squareness ratio ($M_r/M_s$) calculated from the hysteresis loops presented in Fig. 7. For $Co_{0.2}Mg_{0.8}Fe_2O_4$, $M_r/M_s$ was ~0.29, indicating a possible single-domain behavior. The magnetic moment was calculated using the Bohr magneton (Table 7) [17] and decreased with increasing $x$ because of the concomitant drop in the A–B interaction and crystallite size. This lowered the possibility of the presence of multiple domains in nanoparticles. The variation in magnetic permeability and the decrease in magnetic anisotropy constants with increasing $x$ were primarily ascribed to the substitution of the ferromagnetic $Co^{2+}$ ions at octahedral sites with the nonmagnetic $Mg^{2+}$ ions, as evidenced by the concomitant decrease in $M_s$ and the strength of superexchange interactions [20]. The results were compared with those of previous studies (Table 8, Ref [6,16,19]). Magnetocrystalline anisotropy constants were calculated from $M_s$ and $H_c$ and used to determine initial permeability [16].

## 4. Discussion

$Co_{1-x}Mg_xFe_2O_4$ ($x$ = 0, 0.2, 0.4, 0.6, and 0.8) nanoparticles were synthesized through a sol–gel autocombustion method to investigate the effect of $Mg^{2+}$ doping on functional properties. All samples featured the cubic spinel structure (Fd-3m), which indicated that $Mg^{2+}$ substi-

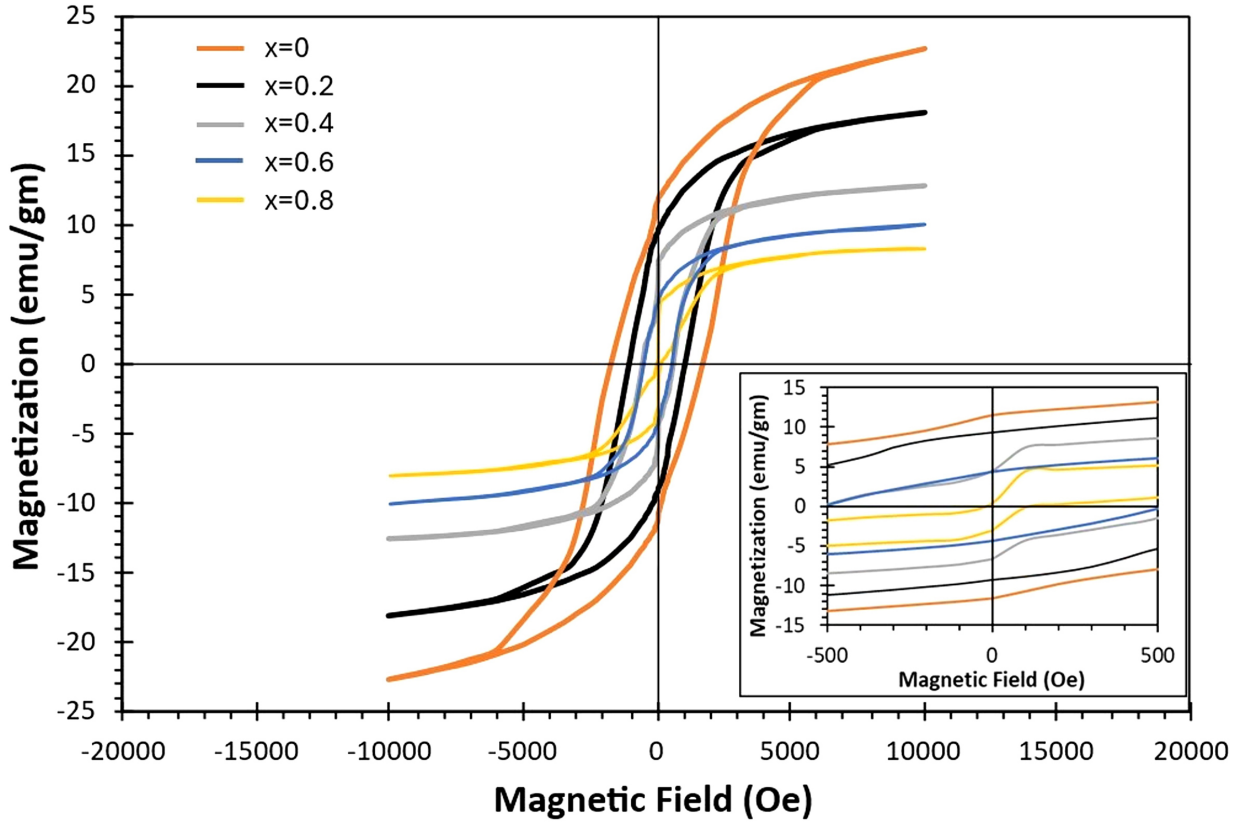


**Fig. 7. Hysteresis loops of $Co_{1-x}Mg_xFe_2O_4$ samples.**

**Table 8. Selected magnetic properties of $Co_{1-x}Mg_xFe_2O_4$ samples determined in previous studies.**

| $x$ | $M_s$ (emu/g) | $M_r$ (emu/g) | $H_c$ (Oe) | $M_r/M_s$ | $\mu_B$ | $\mu_i$ | Reference |
|---|---|---|---|---|---|---|---|
| 0 | 18.08 | 9.31 | 1080.0 | 0.52 | 0.76 | 67.22 | [16] |
| 0.25 | 68.62 | 53.13 | 839.0 | 0.77 | - | - | [6] |
| 0.5 | 38.57 | 31.60 | 667.0 | 0.82 | | | [6] |
| 0.5 | 66.90 | - | 119.9 | - | - | - | [19] |

tuted $Co^{2+}$ with minimal structural disturbance. XRD peak broadening upon doping indicated that $Mg^{2+}$ ions preferentially occupied octahedral sites in the spinel structure. FTIR spectra confirmed the preservation of the spinel structure and featured absorption bands characteristic of tetrahedral- and octahedral-site metal–oxygen bond vibrations. The systematic shift of the latter band with increasing $x$ confirmed the preference of $Mg^{2+}$ for octahedral sites, which caused the reallocation of $Fe^{3+}$ ions across octahedral and tetrahedral sites. Optical absorbance decreased with increasing $x$, which was ascribed to the concomitant weakening of $Fe^{3+}$ and $Co^{2+}$ electronic transitions. The optical bandgap increased from 1.75 eV at $x$ = 0 to 2.30 eV at $x$ = 0.8, which indicates the tunability of the electronic structure and feasibility of optical property control through $Mg^{2+}$ doping. Magnetic property characterization revealed the effect of nonmagnetic $Mg^{2+}$ ions on the magnetic behavior of $Co_{1-x}Mg_xFe_2O_4$. $M_s$, $H_c$, and $K_1$ varied with increasing $x$ because of the substitution of magnetic $Co^{2+}$ ions with nonmagnetic $Mg^{2+}$ ions. In addition, the redistribution of $Fe^{3+}$ reduced its exchange interactions with $Co^{2+}$ and thus also contributed to the abovementioned decrease in magnetic property indicators. The $M_r/M_s$ ratio decreased to <0.5 with increasing $x$. Nanoparticles with $M_r/M_s$ ratios close to 0.1 are likely to be single-domain structures with weak interparticle interactions, which suggests independent reverse field switching. These insights demonstrate that $Mg^{2+}$ doping through sol–gel autocombustion is an effective method for producing structurally stable cobalt ferrite nanoparticles with tunable optical and magnetic properties. Such nanoparticles are useful for optoelectronic and magnetic applications.

*Limitations*

The limitations of this study are mainly associated with the conductive coating used for SEM imaging, which partially obscured fine morphological features, limiting accurate determination of particle size. In addition, elemen-

tal analysis through energy dispersive x-ray spectroscopy was not performed, limiting direct experimental verification of the elemental distribution. The proposed redistribution of $Mg^{2+}$ and $Fe^{3+}$ ions between tetrahedral and octahedral sites was inferred from the combined XRD and FTIR results rather than directly determined using a site-specific characterization technique.

## 5. Conclusions

$Co_{1-x}Mg_xFe_2O_4$ ($x$ = 0, 0.2, 0.4, 0.6, and 0.8) nanoparticles synthesized via a sol–gel autocombustion method retained the cubic spinel structure of $CoFe_2O_4$, demonstrating that $Mg^{2+}$ doping did not disturb the host lattice. The optical bandgap increased from 1.75 eV at $x$ = 0 to 2.30 eV at $x$ = 0.8, indicating that Mg doping enables the tunability of electronic transitions. Saturation magnetization and coercivity decreased with increasing $x$, reflecting the influence of nonmagnetic $Mg^{2+}$ ions and the redistribution of $Fe^{3+}$ ions, which weakened exchange interactions. $Mg^{2+}$ doping modified the structural, optical and magnetic properties of $CoFe_2O_4$, enabling their controllable tuning for optoelectronic and magnetic applications.

## Availability of Data and Materials

All data reported in this paper will also be shared by the lead contact upon request.

## Author Contributions

NAJ, AMZ & GAF designed the research study. NAJ, AKA, AMZ & GAF performed the research. NAJ, AKA, AMZ & GAF analyzed the data. NAJ, AMZ & GAF wrote the manuscript. All authors contributed to editorial changes in the manuscript. All authors read and approved the final manuscript. All authors have participated sufficiently in the work and agreed to be accountable for all aspects of the work.

## Ethics Approval and Consent to Participate

Not applicable.


## Acknowledgment

We gratefully acknowledge the assistance and instruction from all who helped in this work.

## Funding

This research received no external funding.


## Conflicts of Interest

The authors declare no conflicts of interest.

## References


[1] Salih SJ, Mahmood WM. Review on magnetic spinel ferrite ($MFe_2O_4$) nanoparticles: From synthesis to application. Heliyon. 2023; 9: e16601. https://doi.org/10.1016/j.heliyon.2023.e16601

[2] Yadav RS, Kuřitka I, Vilcakova J, Havlica J, Kalina L, Urbánek P, et al. Sonochemical synthesis of $Gd^{3+}$ doped $CoFe_2O_4$ spinel ferrite nanoparticles and its physical properties. Ultrasonics Sonochemistry. 2018; 40: 773–783. https://doi.org/10.1016/j.ultsonch.2017.08.024

[3] Tatarchuk T, Bououdina M, Macyk W, Shyichuk O, Paliychuk N, Yaremiy I, et al. Structural, Optical, and Magnetic Properties of Zn-Doped $CoFe_2O_4$ Nanoparticles. Nanoscale Research Letters. 2017; 12: 141. https://doi.org/10.1186/s11671-017-1899-x

[4] Tong Z, Yao Q, Deng J, Cheng L, Chuang T, Wang J, et al. Effects of Ni-doping on microstructure, magnetic and microwave absorption properties of CoFe2O4. Materials Science and Engineering B. 2021; 268: 115092. https://doi.org/10.1016/j.mseb.2021.115092

[5] Hashim M, Kumar S, Koo BH, Shirsath SE, Mohammed EM, Shah J, et al. Structural, electrical and magnetic properties of Co–Cu ferrite nanoparticles. Journal of Alloys and Compounds. 2012; 518: 11–18. https://doi.org/10.1016/j.jallcom.2011.12.017

[6] Vinayak V, Khirade PP, Birajdar SD, Sable DB, Jadhav KM. Structural, Microstructural, and Magnetic Studies on Magnesium (Mg2+)-Substituted CoFe2O4 Nanoparticles. Journal of Superconductivity and Novel Magnetism. 2016; 29: 1025–1032. https://doi.org/10.1007/s10948-015-3348-3

[7] Mishra B, Munisha B, Nanda J, Sankaran KJ, Suman S. Hydrothermally Synthesized Magnesium Doped Zinc Ferrite Nanoparticles: An extensive study on structural, optical, magnetic, and dielectric properties. Materials Chemistry and Physics. 2022; 292: 126791. https://doi.org/10.1016/j.matchemphys.2022.126791

[8] Melo RS, Silva FC, Moura KR, De Menezes AS, Sinfrônio FS. Magnetic ferrites synthesised using the microwave-hydrothermal method. Journal of Magnetism and Magnetic Materials. 2015; 381: 109–115. https://doi.org/10.1016/j.jmmm.2014.12.040

[9] Ivanova AV, Ivanova EV, Nikitin AA, Cherepanov VM, Abakumov MA. Thermal decomposition of acetylacetonates for highly reproducible synthesis of M-ferrite (Mn, Co and Zn) nanoparticles with tenable magnetic properties. Journal of Alloys and Compounds. 2024; 976: 172737. https://doi.org/10.1016/j.jallcom.2023.172737

[10] Lazarova T, Kovacheva D, Georgieva M, Tzankov D, Tyuliev G, Spassova I, et al. Tunable nanosized spinel manganese ferrites synthesized by solution combustion method. Applied Surface Science. 2019; 496: 143571. https://doi.org/10.1016/j.apsusc.2019.143571

[11] Aisida SO, Ugwu K, Agbogu A, Ahmad I, Maaza M, Ezema FI. Synthesis of intrinsic, manganese and magnesium doped cobalt ferrite nanoparticles: Physical properties for antibacterial activities. Hybrid Advances. 2023; 3: 100049. https://doi.org/10.1016/j.hybadv.2023.100049

[12] Chacko B, Thirumalasetty AB, Vijayakanth V, Wuppulluri M. Optical, Structural, and Magnetic Hyperthermia Properties of Yttrium Iron Garnet Synthesized by Hybrid Microwave-Assisted Hydrothermal and Sol-Gel Auto Combustion Routes. ACS Omega. 2023; 8: 19367–19373. https://doi.org/10.1021/acsomega.3c00162

[13] Adam J, Kumar KV, Kumar NH. Er3+ ion-doped Mg-Zn nanoferrite: Properties and applications in dielectric, magnetic, structural, and optical domains affected by calcination temperature. Inorganic Chemistry Communications. 2024; 167; 112698. https://doi.org/10.1016/j.inoche.2024.112698

[14] Raghasudha M, Ravinder D, Veerasomaiah P. Magnetic properties of Cr-substituted Co-ferrite nanoparticles synthesized by citrate-gel auto combustion method. Journal of Nanos-

tructure in Chemistry. 2013; 3: 63. https://doi.org/10.1186/2193-8865-3-63

[15] Nikam PN, Patil SS, Chougale UM, Fulari AV, Fulari VJ. Supercapacitor properties of Ni2+ incrementally substituted with Co2+ in cubic spinel NixCo1-xFe2O4 nanoparticles by sol-gel auto combustion method. Journal of Energy Storage. 2024; 96: 112648. https://doi.org/10.1016/j.est.2024.112648

[16] Jaber NA, Zaki AM, Fadhil GA. Study Phase Structure, Cation Distribution and Magnetic Properties of Cobalt, Magnesium and Copper Ferrites. Surface Review and Letters. 2026; 33: 2550103. https://doi.org/10.1142/S0218625X25501033

[17] Monisha P, Priyadharshini P, Gomathi SS, Mahendran M, Pushpanathan K. Role of Zn dopant on superparamagnetic property of CoFe2O4 nanoparticles. Applied Physics A: Materials Science & Processing. 2019; 125: 736. https://doi.org/10.1007/s00339-019-3014-x

[18] Mohanty D, Naik AU, Nayak PK, Behera B, Satpathy SK. Structural and Electrical Properties of Magnesium-Doped CoFe2O4. Powder Metallurgy and Metal Ceramics. 2021; 59: 507–514. https://doi.org/10.1007/s11106-021-00190-9

[19] Mokhosi SR, Mdlalose W, Mngadi S, Singh M, Moyo T. Assessing the structural, morphological and magnetic properties of polymer coated magnesium-doped cobalt ferrite (CoFe2O4) nanoparticles for biomedical application. Journal of Physics: Conference Series. 2019; 1310: 012014. https://doi.org/10.1088/1742-6596/1310/1/012014

[20] Salih SJ, Abd Ali LI, Hamad WM. Novel synthesis and characterization of magnesium-doped CoFe2O4 nanoparticles-SiO2-3-aminopropylethoxysilane-gallic acid magnetic nanocomposite for effective removal of cationic dyes. Arabian Journal of Chemistry. 2024; 17: 105647. https://doi.org/10.1016/j.arabjc.2024.105647

[21] Ivanova O, Edelman I, Thakur P, Molokeev M, Zharkov S, Knyazev Y, et al. Transition from soft to hard ferrite in Co1-xMgxFe2O4 nanoparticles: Cation distribution, magnetic and magneto-optical properties. Journal of Magnetism and Magnetic Materials. 2026; 651: 174180. https://doi.org/10.1016/j.jmmm.2026.174180